Upgrade of JCNS SANS instrument KWS-2 for improved performance and beam-time efficiency

Aurel Radulescu[1*], *Jia-Jhen* Kang[1], *Marie-Sousai* Appavou[1], and *Aristeidis* Papagiannopoulos[2]

[1]Jülich Centre for Neutron Science (JCNS) at Heinz Maier-Leibnitz Zentrum (MLZ), Forscungszentrum Jülich, 85748 Garching, Germany

[2]Theoretical and Physical Chemistry Institute, National Hellenic Research Foundation,11635 Athens, Greece

Abstract. KWS-2 is a classical small angle neutron diffractometer where, following recent upgrades, the pinhole mode with different neutron-wavelengths and detector distances can be combined with focusing mode with MgF_2 lenses to reach a wide Q-range between $2x10^{-4}$ and 1.0 Å^{-1}. Further upgrades of the detection system and sample positioning system are currently in progress. A wide-angle detection prototype is currently being tested and optimized aiming at measurement conditions over an extended Q-range up to 2.0 Å^{-1}, which will be beneficial for semi-crystalline materials and small biological morphologies. The high neutron flux provided by the FRMII reactor and transported by the optimized neutron guidance system requires an adjustment of the measurement routine for a more rational use of the beam time. A new versatile in-beam sample positioning system, which includes a multi-position carousel with temperature control, robotic elements, and a storage pool for sample cuvettes, has just been installed at the instrument's sample position. This allows the instrument to be continuously supplied with samples and provides the ability to combine experiments on similar samples or topics into a common long experimental session. Here we report in detail on the expanded Q-range option of the KWS-2 from the perspective of current performance and planned upgrades, as well as the new sample positioning system with robotic elements.

1 Introduction

The understanding of soft- and bio-materials, such as semi-crystalline polymers in melt and solution, block copolymer assemblies, polymer gels and membranes, or proteins, polysaccharides and lipids complexes, requires the global knowledge of their microstructural features on a wide length scale between several Å and μm sizes. Such a wide length scale can be explored at the KWS-2 small-angle neutron (SANS) diffractometer of Jülich Centre for Neutron Science (JCNS) at Heinz Maier-Leibnitz Zentrum (MLZ) [1-5].

KWS-2 instrument is designed for high intensity studies of the mesoscopic structures with their local conformation order and long-range assemblies and correlations and their changes due to kinetic processes under various stimuli, such as temperature, hydration level, deformation, rapid mixing, etc., in the fields of soft condensed matter, chemistry, and biology. The instrument was recently optimized for structural investigations over a wide momentum transfer Q range, between $2x10^{-4}$ Å^{-1} and 1.0 Å^{-1}, by combining classical pinhole and focusing (with neutron lenses) methods, while simultaneously providing high-neutron intensities with an adjustable resolution – $\Delta\lambda/\lambda$ between 2% and 20%, using a versatile velocity selector in combination with a primary double-disc chopper with variable slit opening and TOF data acquisition [3]. A secondary single-disc compact chopper is available at the sample position and allows for the separation of the inelastic and elastic scattering with consequence in reducing the incoherent background from hydrogenated samples [5].

To further improve instrument performance and beam time efficiency, new upgrades to the detection system and sample environment are currently under development. A wide-angle detection option is currently in the installation phase and will allow measurements over an extended Q-range of up to 2.0 Å^{-1}, which will be beneficial for the characterization of semi-crystalline materials and small biological morphologies. In addition, the high neutron flux demanded optimization of the measurement procedure to make the best use of the beam time. A new versatile sample positioning system in the beam, which includes a thermostated multi-position carousel, robotic elements, and a storage pool of sample cuvettes has just been installed at the instrument's sample position. This allows a continuous supply of samples to the instrument and the pooling of experiments from different user teams when similar experimental conditions are required. In this paper, we focus on the extended Q-range measurement approach on the instrument and report on combined simulations by McStas and proof-of-principle measurements to provide a comprehensive understanding of the instrument's capabilities in terms of characterizing structures and morphologies over a large length scale, including the current status and expected performance due to ongoing upgrades.

* Corresponding author: a.radulescu@fz-juelich.de

2 The Q-range of KWS-2

2.1 Methodical aspects

The information in the elastic scattering experiments with neutrons is contained in the neutron intensity measured as a function of the momentum transfer Q:

$$Q = \frac{4\pi}{\lambda} \sin\theta$$

where λ is the neutron wavelength and 2θ is the scattering angle. Aiming for mesoscopic scale, SANS is optimized for observation at small angles and thus large scattering objects. A figure of merit of such kind of instrument is the Q-range that can be covered, thus the scale of lengths that can be characterised in real space. Typically, in pinhole SANS instruments at a reactor source for routine experiments, a specific wavelength corresponding to the maximum flux on the sample is selected from the broad flux distribution transported by the neutron guide system. This defines the typical Q-range that the instrument can cover by performing a series of measurements in which the detector is placed at different predefined positions after the sample so that a wide angular range 2θ can be scanned. Shorter and longer wavelengths can be used to complement the measurements, depending on the method used for obtaining monochromatic beams, and available flux at the instrument, pushing Q_{max} to higher values (for shorter λ) or Q_{min} to lower values (for longer λ). For KWS-2, $\lambda = 5$ Å is routinely used, allowing a Q range between 0.002 and 0.55 Å^{-1} to be covered in routine experiments, since the detection length L_D can be varied between 1.0 m and 20.0 m downstream of the sample. Since the velocity selector (Astrium GmbH) can be operated at different velocities and inclination angles against the beam direction, neutrons with $\lambda = 2.8$ Å and 10.0 Å can be used complementarily to extend the Q range in pinhole mode from 0.001 to 1.0 Å^{-1}. Tilting of the selector with respect to the beam axis enables the shift of the λ_{min} from 4.5 Å in the standard configuration to 2.8 Å. However, tilting of the velocity selector is a two-ways approach: the provision of shorter wavelengths compared to the standard configuration is accompanied by the worsening of the $\Delta\lambda/\lambda$ wavelength spread and the limitation of the largest wavelength available. Thus, the velocity selector in operation at KWS-2 delivers a monochromatic λ in the range 4.5 - 20 Å with a $\Delta\lambda/\lambda = 10\%$ when it is operated in the standard configuration, with its axis parallel to the beam axis, and with rotation speeds within the range 8000 – 28200 rpm, while when used in a tilted configuration with the tilting angle $\xi_i = -10°$ against the beam axis, the λ range is shifted to 2.8 – 7 Å with $\Delta\lambda/\lambda$ between 14% and 18.5%, for the same range of rotation speed. Larger values than $\lambda = 7$ Å in the tilted configuration are prohibited due to vibrations from resonance frequencies of the selector.
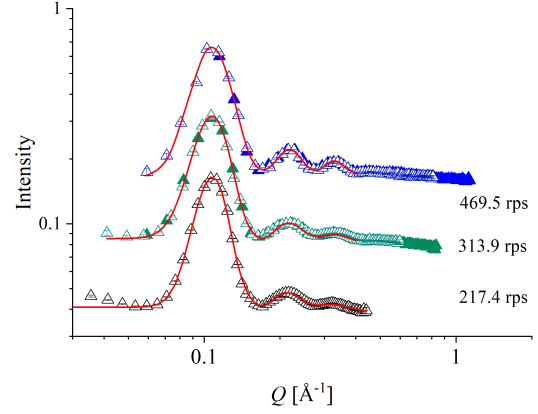

Fig. 1. Experimental SANS data (symbols) for the reference AgBeh sample measured on KWS-2 at an L_D of 1.0 m (full symbols) and 1.60 m (open symbols), with the velocity selector positioned at inclination angle of −10° with respect to the beam axis and operated at different rotation speeds (expressed in rotation per second units). The fit of the data (red lines) delivered the λ and the $\Delta\lambda/\lambda$ values reported in Table 1.

Fig. 1 presents the scattering patterns from AgBeh measured in the high Q regime at KWS-2 at different L_D and using the velocity selector at different rotation speeds, in inclined configuration. AgBeh is a wavelength calibrant used in small angle scattering experiments with X-rays and neutrons. The Bragg spacing of AgBeh is known to be $d_{AgBeh} = 58.38$ Å [6, 7]. AgBeh can also be used as reference material for determining the instrumental resolution parameters, as shown in [8], when Bragg peaks with several orders are observed at large angles (thus at $Q \geq 0.1$ Å^{-1}). In this range the uncertainty in Q is mainly governed by the wavelength spread $\Delta\lambda/\lambda$. The peak analysis of the scattering patterns shown in Fig. 1 was done by a simultaneous fit of the three observed peaks in all scattering patters measured with the same λ according to the equation

$$I_{AgBeh}^{model}(Q) = \sum_{i=1}^{N} \frac{A_i}{\sqrt{2\pi}\,\Delta Q(Q)} exp\left(-\left[\frac{Q-Q_i^{peak}}{\sqrt{2}\,\Delta Q(Q)}\right]^2\right) + bckd$$

with A_i – the area of the peak, N – the number of observed peaks, which was always 3, and $bckd$ a constant background describing the flat behavior of the scattering patterns at high Q. The $(\Delta Q(Q))^2$ was considered as a sum of the wavelength and the geometrical terms of the Q resolution [3], namely $(\Delta Q_\lambda)^2$ – the wavelength spread term that depends on $\Delta Q_\lambda = Q\,\Delta\lambda/\lambda$, and $(\Delta Q_{geo})^2$ – the geometrical term that depends on the experimental conditions such as collimation and detection lengths, apertures sizes, etc. [3]. Because ΔQ_{geo} was known, it was considered fixed parameter in the analysis, while $\Delta\lambda/\lambda$ was considered variable parameter and was thus delivered by the fitting procedure, as reported in Table 1. The effect of the wavelength cut-off shown by the neutron guide system at KWS-2 [2] is clearly observable in the variation of the

$\Delta\lambda/\lambda$, which increases in increasing the λ between $\Delta\lambda/\lambda$ of 14% and 18.5%.

Table 1. KWS-2 velocity selector parameters tilted under the angle $\xi_i = -10°$ against the beam axis: the rotation speed, the wavelength and the wavelength spread.

Speed [rps]	λ [Å]	$\Delta\lambda/\lambda$ [%]
469.5	2.8	14.0
313.9	4.0	16.5
217.4	5.0	18.5

For lower Q values, pinhole operation can be supplemented by focusing mode: a package of MgF_2 lenses can focus a small entrance aperture (typically 4 x 4 mm²) placed 18.5 m in front of the lens system onto a two-dimensional high-resolution scintillation detector (HRD) with 1.0 mm position resolution placed 18.5 m behind the lens system, so that neutrons scattered from a sample placed immediately behind the lenses can be detected at a much smaller angle than in pinhole operation. The small entrance aperture and the HRD are placed in fixed positions in the two focal points of the lens system, thus at 20 m and 17.0 m in front and after the sample, respectively. The focusing operation mode at KWS-2 is schematically depicted in Fig. 2 together with the conventional pinhole mode.

At KWS-2 26 MgF_2 lenses with a diameter $\Phi = 5$ cm and a parabolic shape, to avoid geometrical aberrations [9], are operational. The lenses can be grouped in different packages, to match the focusing conditions for different wavelengths λ in the configuration of entrance aperture – sample position – HRD which is mentioned above and schematically shown in Fig. 2. Thus, for $\lambda = 17.5$ Å, 4 lenses, for $\lambda = 11$ Å, 10 lenses, and for $\lambda = 7$ Å, 26 lenses are used, respectively. The lenses are kept at 77 K, to increase the transmission due to decrease in the scattering on phonons in the lens material [9]. The measured transmission of 26 lenses at room temperature was about T = 32%, when the full lens area was used, thus a circular sample aperture of 5 cm diameter was placed after the lens system. The transmission increased to T = 65% when lenses were used at 77 K, while in the same condition, but with only 1 cm x 1 cm beam size after the lens system, more realistic for routine applications, the transmission was T = 92%. For an entrance aperture of 4 mm x 4 mm at 20 m in front of the sample position, a neutron flux of 10^4 n s^{-1} cm^{-2} for $\lambda = 7$ Å and 600 n s^{-1} cm^{-2} for $\lambda = 17.5$ Å was estimated on the sample, respectively, by measuring the transmitted beam on the HRD detector and taking into account the detector efficiency of about 95%, which was considered constant for this wavelength range. If one multiplies the neutron flux estimated for $\lambda = 7$ Å when lenses are in beam with the ratio between the entrance aperture size (4 mm x 4 mm) and the cross-section of the guide feeding the instrument (50 mm x 50 mm) and normalizes the obtained value to the lens transmission, one can find a nominal neutron flux of 1.7 x 10^6 n s^{-1} cm^{-2}, which is pretty much the measured neutron flux on the sample position for $\lambda = 7$ Å at a collimation length of 20 m [2]. The same calculation holds for $\lambda = 17.5$ Å. This shows the good neutron transmission of the lens system.
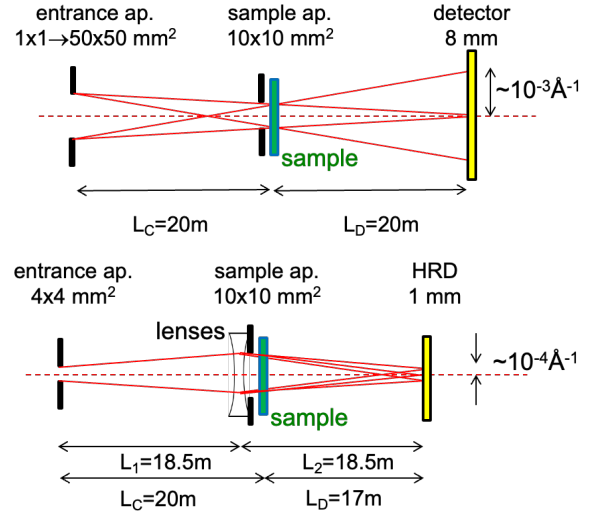

Fig. 2. Schematic presentation of the pinhole (top) and focusing (bottom) operation modes at KWS-2. The main technical elements and dimensions are indicated.

Lenses are focusing ideally only the central wavelength in the broad $\Delta\lambda/\lambda$ that is delivered by the velocity selector. A large wavelength spread yields on the detector a "peanut like" transmitted beam, due to defocusing of shorter and longer wavelengths and gravity effects. To tackle this effect, the quality of the transmitted beam by the lens system was checked on a first attempt for a longer neutron wavelength, $\lambda = 17.5$ Å, and a broad wavelength distribution $\Delta\lambda/\lambda = 20\%$ first on the main detector at KWS-2, which was placed at $L_D = 17.0$ m, in the image focal point of the lens system, then on the HRD, at the same distance after the sample. Fig. 3 shows the transmitted beam with $\lambda = 17.5$ Å and $\Delta\lambda/\lambda = 20\%$ through the lens system, so with 4 lenses in beam, as collected on the main detector (resolution 8 mm). The "peanut like" shape of the direct beam can be easily recognized on the left side panel presenting a sector of the detector. When the beam is analysed in TOF mode by using the resolution chopper [3], the broad distribution $\Delta\lambda/\lambda = 20\%$ delivered by the selector is split into narrower slices and several beams with slightly different λ, each characterized by the narrow distribution $\Delta\lambda/\lambda = 5\%$, are recorded on the detector at different TOF. As shown in the other panels of Fig. 3 the gravity effect is clearly recognized due to the vertical distribution of these narrow beams that are characterized by an isotropic geometrical shape: the longer the λ, the lower the beam positioning on the detector.
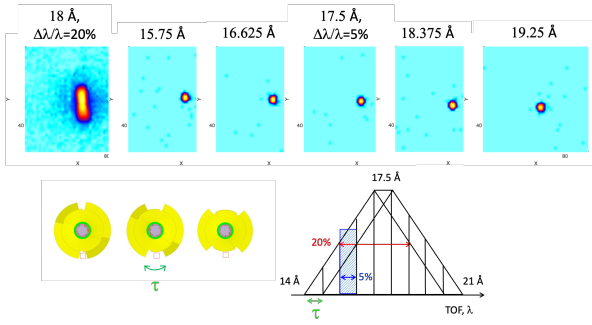
Fig. 3. The profile of the direct beam through the 4-lens system for $\lambda = 17.5$ Å and $\Delta\lambda/\lambda = 20\%$ measured in standard (upper left panel) and TOF (other upper panels) data acquisition modes, when different λ with $\Delta\lambda/\lambda = 5\%$ were sorted out from the initial broad wavelength distribution (lower right scheme) by setting the proper opening time τ of the chopper slit (lower left scheme).

Results of McStas simulations of the direct beam transported through the full guide system of KWS-2 and the system of lenses and detected at $L_D = 17.5$ m after the sample position on a two-dimensional detector (pixel size = 0.5 mm) are reported in Fig. 4 as detector images and wavelength distributions at the detection positions in the graphical format delivered by the simulation package. The simulations were carried out with a 20 m collimation length with a small entrance aperture (4 mm x 4 mm) and a 15 mm x 15 mm sample aperture for different wavelengths and wavelength distributions. The McStas component lens.comp (spherical lens, diameter $\Phi = 2.5$ cm) was used in the simulation. Fig. 4a,g report the direct beam image when lenses are out of beam for $\lambda = 17.5$ Å and $\lambda = 7$ Å, always with $\Delta\lambda/\lambda = 20\%$, while Fig. 4d,i show the wavelength distribution computed at the detection position. The effect of lenses on the beam profile is observed in Fig. 4b,c for $\lambda = 17.5$ Å (4 lenses in beam) with $\Delta\lambda/\lambda = 20\%$ and 5%, respectively, with the corresponding wavelength distribution shown in Fig. 4e,f. Fig. 4h,j report the beam profile and wavelength distribution computed at the detection position for $\lambda = 7$ Å (26 lenses in beam) with $\Delta\lambda/\lambda = 20\%$. In parallel, the measured direct beam for $\lambda = 17.5$ Å with $\Delta\lambda/\lambda = 20\%$ and 5% (in TOF mode), are presented in Fig. 4k,l. Focusing effect induced by lenses is clearly observed when compared the results to those obtained for the lenses free instrument. Also, the gravitational and polychromatic effects are obvious in case of using the lenses for focusing the long wavelength $\lambda = 17.5$ Å with a broad wavelength distribution $\Delta\lambda/\lambda = 20\%$: while the focusing is achieved on the horizontal beam spot dimension, the vertical spot dimension is still large, comparable to the lenses free vertical size of the beam. When the wavelength distribution is narrowed down to $\Delta\lambda/\lambda = 5\%$, beam focusing is obtained in both directions. The effect is observed in both simulated and measured results, and is striking in the case of the shorter wavelength $\lambda = 7$ Å even for the broader wavelength distribution $\Delta\lambda/\lambda = 20\%$. We can add that the

experimental background observed in Fig. 4k,l outside of the direct beam spots is due to the γ-sensitivity (10-4) of the scintillation-type HRD, which however does not affect the quality of the measured data, when proper corrections for the detector sensitivity, "dark current" and empty sample container are applied.

The good agreement between the simulation of an ideal instrumental setup and the measurement carried out in similar conditions proves the normal behavior of the lens system at KWS-2.
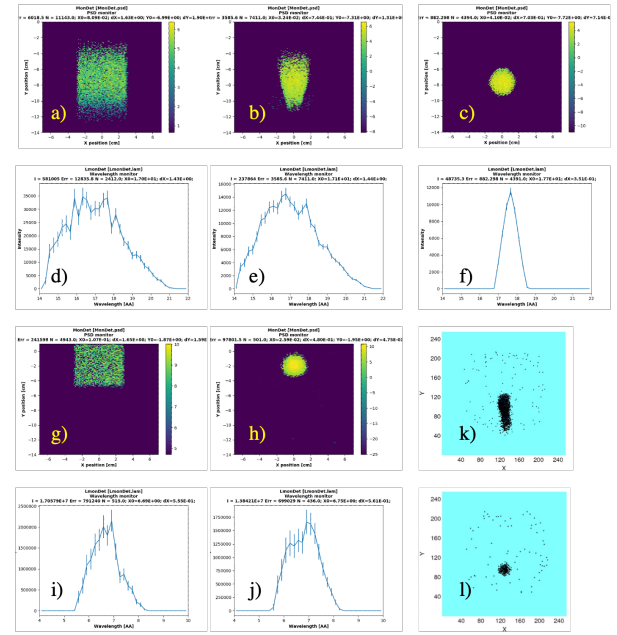

Fig. 4. Results of McStas simulations (taking into account the gravity) and neutron measurements of the direct beam profile on the detector placed at 17.5 m for 4-lens system in beam. Panels a) and g) show the direct beam on the detector when lenses are out of beam for $\lambda = 18$ Å and $\lambda = 7$ Å, respectively, for a $\Delta\lambda/\lambda = 20\%$ in both cases, while panels e) and g) present the wavelength distribution in both situations. Panels b) and c) show the direct beam on the detector when lenses are in beam, for a $\Delta\lambda/\lambda = 20\%$ and $\Delta\lambda/\lambda = 5\%$, respectively, while panels e) and f) present the corresponding wavelength distribution. Panels h) and j) present the same data for $\lambda = 7$ Å with a $\Delta\lambda/\lambda = 20\%$. Panels k) and l) show measured direct beam profile on the HRD for $\lambda = 18$ Å, with $\Delta\lambda/\lambda = 20\%$ and $\Delta\lambda/\lambda = 5\%$ (using TOF mode).

2.2 Current performance

With its high flux [4], comparable to that of the world's leading pinhole SANS instruments, and its extended Q-range between 2×10^{-4} Å^{-1} and 1.0 Å^{-1}, which can be covered by combining pinhole and focusing modes, KWS-2 is a high-throughput instrument that typically measures a large number of samples during short experiments. As an example of typical experimental results, Fig. 5 shows scattering patterns recorded at room temperature over the entire Q range currently available at the instrument from samples representative of those characterized on the KWS-2: a sample consisting of a uni-lamellar vesicle (ULV)

forming mixture of lipid molecules in D_2O buffer solution (Fig. 5a), showing adhesion (docking) effects when myelin basic protein (MBP) is added to the solution (Fig. 5b), resulting in vesicle assemblies and multilamellar domains, as nicely shown by the cryo-TEM image in Fig. 5b. The detailed sample composition and preparation protocols as well as the experimental procedure and data analysis are reported elsewhere [10]. Here, only the experimental details related to the methodological approach and beam time efficiency are discussed to support the currently ongoing instrument developments.

SANS measurements on the sample with mixed lipids in D_2O buffer solution (Fig. 5a) were performed in pinhole mode using $\lambda = 5.0$ Å with $L_D = 2$ m and 8 m, and $\lambda = 10.0$ Å with $L_D = 20$ m. For all experimental conditions, $\Delta\lambda/\lambda$ was 10% (standard selector configuration). The lipid molecules lead to the formation of ULVs as shown by cryo-TEM observation (inset in Fig. 5a). The scattering pattern in Fig. 5a is well described by the vesicle form factor (indicated by the red line) and shows all the typical scattering features of a vesicular morphology: the total size of vesicles, indicated by the Guinier plateau observed at low Q, and the thickness of the vesicle bilayer, indicated by the deviation of the intensity from the Q^{-2} power law characteristic of the two-dimensional bilayer morphology. It is also worth noting that SANS measurements performed with a higher lipid concentration in solution did not show vesicle aggregation and the scattering features of individual ULVs were still clearly observed [10]. The data acquisition time was 10 min for $L_D = 2$ m and 8 m, and 15 min for $L_D = 20$ m, respectively. According to our experience and the opinion of our users, the acquisition time for such samples is comparable to that at other high-flux pinhole SANS diffractometers such as the D22 at ILL-Grenoble. When MBP is added to the ULV solution, much larger morphologies are formed, as no Guinier regime of vesicle size is detectable anymore in the scattering pattern measured in standard pinhole mode. The SANS pattern was completed with measurement at very low Q, using the focusing mode with $\lambda = 7.0$ Å and 26 MgF_2 lenses in the beam, while data were collected on the HRD instrument for data acquisition in standard mode (not TOF mode) over a measurement time of 15 minutes. In the extended scattering pattern, a Guinier regime was observed at about an order of magnitude lower Q compared to the ULV solution case. In addition, two broad maxima, indicated by the vertical arrows in Fig. 5b, are observed at intermediate and high Q values. The Guinier regime observed at very low Q in the case of the MBP-doped vesicle solution indicates the formation of vesicle aggregates characterized by a radius of gyration about ten times larger than that of the ULVs themselves, as also shown by the cryo-TEM images, an effect attributed to the addition of MBP to the solution after ULV formation. Relying on the cryo-TEM observations and the model interpretation of the scattering data (red line in Fig. 5b) based on a partitioning between single and docked ULVs (blue line) as described in [11],

combined with a Beaucage form factor [12] of the large-scale vesicle aggregates, we report here only the nature of the two broad maxima clearly seen in Fig. 5b: the higher Q maximum is due to vesicle adhesion (docking) mediated by the MBP, which promotes a local multi-lamellarity effect and the formation of larger vesicle aggregates, while the intermediate Q maximum is a detail of the vesicle form factor accentuated by the additional scattering due to vesicle aggregates at low Q, which overlaps the form factor of the ULVs.
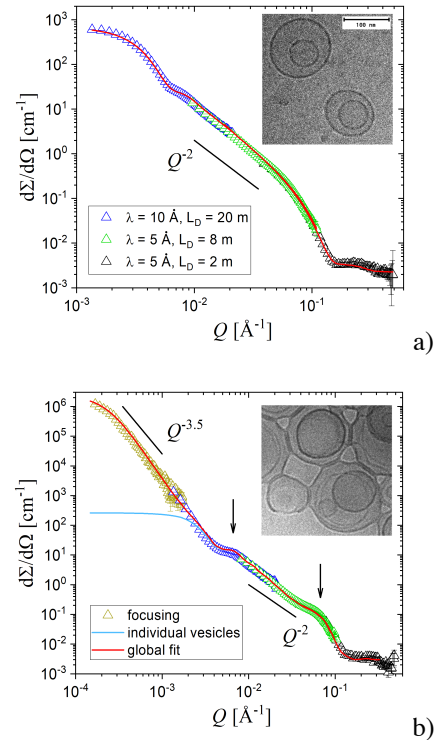

a)

b)

Fig. 5. SANS data of lipid (a) and lipid + MBP (b) solutions recorded at KWS-2 in pinhole mode (a) and in combined pinhole and focusing modes (b). The red curves show the model fit of the experimental data according to the vesicle form factor (a) and the unified model of the docked vesicles, as the product of vesicle form factor and docking structure factor, and the large-scale aggregates (b). The light blue curve in panel (b) shows the scattering contribution of the docked vesicles. The insets show cryo-TEM images of the same samples, where the scale bar valid for both images is 100 nm.

Thus, experimental studies as described in Fig. 5a,b can be performed in a very short time at the KWS-2, and it typically takes up to one hour per sample to cover the entire Q range between 2.0×10^{-4} and 1.0 Å^{-1} using the combination of pinhole and focusing modes. The total estimated time for a complete measurement of a sample also includes the time lost by reaching different instrument configurations. The most time consuming is the movement of the main detector between different detection positions L_D and the time needed to move the HRD in the beam, while the lenses can be moved in or out of the beam in a few seconds, as well as all other elements such as collimation apertures and guide segments or the beam-stop, which has to be repositioned according to the λ and L_D conditions. It is also worth

mentioning that the selection of a new λ via the velocity selector is done simultaneously with the main detector movement, so no additional time is lost by this adjustment. The versatile NICOS [13] instrument control software allows optimization of complex experimental protocols, including pinhole and focusing settings, reducing time-consuming adjustments during the investigation of a full set of samples. As with any other SANS diffractometer, whether it is a pinhole or TOF instrument, most of the lost time at KWS-2 is due to changing samples or the experimental team at the instrument. Therefore, one of the upgrades currently underway aims to change the concept of sample delivery to the instrument to use the beam-time more efficiently, and will be discussed in more detail in the next section.

Finally, it should be mentioned that an extended Q-range structural study at lower Q-values towards 10^{-4} Å^{-1} is currently used routinely only at a very limited number of SANS pinhole instruments besides KWS-2, namely SANS-J-II at the JRR-3 reactor, Tokai, Japan [14], with neutron lenses and HRD, and QUOKKA at ANSTO, Australia [15], with neutron lenses but without HRD. To our knowledge, no TOF-SANS instrument operating at research reactors or spallation sources can cover such a wide Q range down to these low Q values. Although some TOF-SANS instruments at spallation sources can cover a very wide Q range in a single measurement without requiring a configuration change, such as the BL-15 TAIKAN at J-PARC, which uses a broad range of wavelengths along with a large number of detectors in fixed positions so that a wide angular range in scattering can be covered [16], the Q_{min} achieved at such instruments is nevertheless much larger than that achieved at KWS-2 with the combined pinhole focusing modes. Most TOF-SANS instruments at spallation or steady-state (reactor) neutron sources, such as SANS-2D at ISIS, UK [17], EQ-SANS at SNS, USA [18], D33 at ILL-Grenoble, France [19] or BILBY at ANSTO, Australia [20], use mobile main detectors. Therefore, a combination of different experimental setups must be used to cover the specified Q range, which translates into a long acquisition time per sample comparable to the time required at KWS-2. However, none of these instruments can achieve a Q_{min} value of less than 1.0×10^{-3} Å^{-1}. Pinhole SANS instruments at reactors using a complementary focusing method are far superior to these instruments in terms of extended Q range toward lower Q values. On the other hand, the advantage of TOF-SANS instruments, which use a broad wavelength band, is the ability to cover an extended Q range with higher Q values than pinhole instruments. Some of these instruments, such as BL-15 TAIKAN at J-PARC, can reach Q values up to several Å^{-1}. As we have just reported [21], the ability to cover a Q range up to 2.0 Å^{-1} offers unique advantages in the characterization of semi-crystalline polymer systems under application-relevant conditions using the neutron contrast variation method. Several pinhole or TOF instruments are already equipped with wide-angle detectors to cover higher Q values than the usual Q range. Therefore, another ongoing upgrade at KWS-2, presented in the next section, is the installation of a

wide-angle detector system to increase the instrument performance up to $Q_{max} = 2.0$ Å^{-1}.

2.3 Developments in progress

A fully automated sample exchange and positioning system was developed for KWS-2 to allow continuous supply of samples to the instrument while minimizing sources of error and scientist involvement in sample positioning, and to provide the ability to pool experiments from different user teams when similar experimental conditions are required.
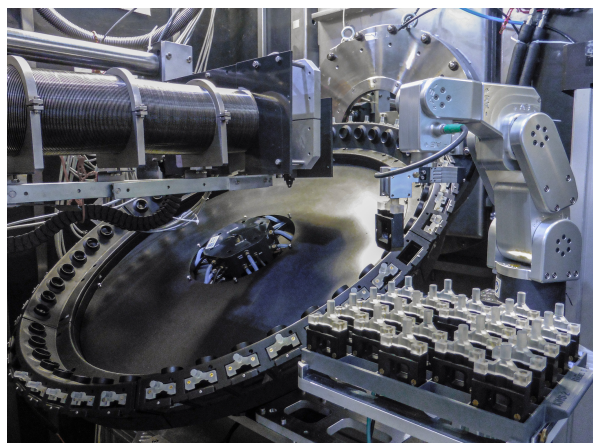

Fig. 6. The fully automated new sample positioning system at KWS-2, including the multi-position sample carousel, the robotic arm and the cuvette storage pool.

The new system, which includes a multi-position carousel with sample temperature control, robotic elements and a storage pool for sample cuvettes, was installed in the sample area (Fig. 6). The new compact setup will remain in operation at the sample area as a standard option for all routine experiments, i.e. about 80% of the beam time at KWS-2. For the remaining experiments requiring more specialized sample environments such as rheometers, stop-flow devices, pressure or humidity chambers, the ease of removal and precise repositioning by a zero-point clamping system will allow a smooth change of options. A 48-position COLOSSUS sample carousel (Quantum Northwest Inc., Liberty Lake, WA) with temperature controllers was installed on the sample table (Fig. 6). The instrument is divided into six sections, each with 8 positions. Each section is equipped with two Peltier elements and a temperature controller so that the sections can be controlled independently. This allows up to six temperatures between 5 °C and 110 °C to be set simultaneously on different samples, with a precision of 0.01 °C, an accuracy of 0.5 °C and a temperature reproducibility of 0.05 °C in the temperature interval from 5 °C to 80 °C. The geometry of each sample chamber equipped with quartz windows has been designed to allow an angular range for dispersion greater than ± 50 °C. Mechanical control and temperature regulation are provided by the KWS-2 control software NICOS [13]. The instrument is designed to hold Banjo

quartz cuvettes in special Al carriers, which are moved by a robotic arm between COLOSSUS and a nearby cuvette storage pool. A nearly continuous supply of samples to the instrument is ensured by regular refreshing of the cuvette storage pool by the experimentalist when the ongoing experimental routine allows this without loss of time, e.g. during the movement of the main detector between different positions L_D, which takes several minutes. Loading and unloading of the COLOSSUS with sample cuvettes from the cuvette storage is performed by a compact six-axis Meca500 robotic arm (Mecademic Inc, Canada) equipped with an electric parallel gripper MEGP 25LS (Fig. 6). A proof-of-principle of the new sample changing concept at KWS-2 can be seen in [22]. With the COLOSSUS, the robotic arm and the cuvette storage pool installed at the sample position, a nearly fully automated instrument supply of samples is possible at the KWS-2. At least 96 samples can be measured without interruption, which, taking into account the foreseen temperature variations at the sample, means that almost a week of beam-time can be spent at the instrument without the need for the instrument or guest scientists at the sample position. Renewal of the cuvette storage pool is easily possible at any time, as mentioned above, which further increases the degree of freedom. In our experience, an estimated 3-4 experiments of the same type can be pooled, minimizing the lost time and improving the beam-time planning at the instrument.

To further improve the performance of the instrument, a wide-angle detection option has just been tested and optimized to enable measurements over an extended Q-range of up to 2.0 Å^{-1}. This will be beneficial for the characterization of semi-crystalline materials and small biological morphologies. In 2015, a new high count rate detection system was commissioned at KWS-2 [4]. This system consists of an array of 144 position-sensitive ^{3}He detection tubes (PSDs) and fast readout electronics, providing high count rates up to several MHz, high count stability and, based on the large detection area (almost 1.0 m^2, with a diamond shape for optimal filling of the vacuum tank cross-section), measurements up to $Q_{max} = 1.0$ Å^{-1} at $\lambda = 2.8$ Å, with a resolution $\Delta\lambda/\lambda = 14.5\%$. However, as reported in [21], an efficient combined SANS/WANS approach on the same instrument with the ability to use contrast variation to obtain comprehensive information on hydrocarbon systems under conditions relevant to the application would require a Q_{max} of at least 2.0 1.0 Å^{-1} at KWS-2. Therefore, the installation of a WANS option at KWS-2 is currently in progress. Given the great versatility of the instrument, which is equipped with two types of chopper systems, the resolution double-disk chopper [3] and the background single-disk chopper [5], WANS and SANS measurements at KWS-2 will be aimed at in various combinations of standard and TOF modes.

Considering the instrument concept and the available conditions in the FRM II reactor guide hall, two large-area detector wings are currently being designed to be installed in inclined fixed positions behind the sample (Fig. 7), so that the scattered neutrons can be detected in a wide angular range up to $2\theta_{max} =$ 50°. The two detector wings are placed above and below the beam axis at a distance of 1.25 m downstream of the sample position, which provides the possibility to record the scattered neutrons in the high-Q region of the instrument in TOF mode, if required, and to discard the inelastic component from the measured data to improve the signal-to-noise ratio at the instrument, as described in [5]. Each wing consists of an array of 80 ^{3}He PSDs. The PSDs have a thickness of 6 mm and an active length of 60 cm and are supplied by Canon Electronics Tubes and Devices Inc. (CETD), Japan, along with fast readout electronics that can operate in vacuum (better than 0.002 mbar, as recommended by the manufacturer) or in air or He atmosphere. The latter configuration would not require a cooling system for the readout electronics, as demonstrated by the use of the same detection system for the WANS detection banks of the BL-15 TAIKAN, J-PARC [16], and would help avoid technical complications associated with operation in vacuum. A prototype of such a detection module (an 8-pack of PSDs) was tested at MLZ in Garching using a stationary ^{252}Cf neutron source and a borated mask with narrow slits. The test resulted in the expected position resolution of about 4-5 mm in the middle and at the end of the PSD tubes. A schematic representation of the proposed WANS option operating complementary and simultaneously with the SANS option at KWS-2 is shown in Fig. 7, where the sample location (1), the fixed WANS panels (2), the movable SANS detector (3), and the He-boxes (4) can be easily identified. In the final concept of the WANS option, the WANS detectors are operated in the air with He-boxes installed in front of them so that the air path between the sample and the PSDs is minimized. By using He gas at a pressure of 1 bar inside the boxes, very thin Al windows can be used at the entrance to the sample and at the exit to the PSD array, keeping the background at a very low level. A detailed discussion of the background sources in SANS experiments, including the air path at the sample position and the windows, and how their contribution can be minimized can be found in [23]. This measurement geometry also allows optimization of the pyramid-shaped nose of the main detector vacuum tank so that a smaller and thinner Si entrance window than the actual one can be installed to maintain the large pressure difference between the ambient pressure at the sample position and the 10^{-2} mbar vacuum in the tank. In this experimental configuration, a large vacuum shutter is no longer needed, which will simplify the technical implementation of the WANS option and the operation of the instrument during the routine user program. It is planned to install mechanical external shields that can be moved in and out of the window front and be interlocked with the condition of the access lead shielding door, so that damage to the windows can be avoided during activities at the sample position. In this configuration, the closest position of the main SANS detector to the sample position is $L_D = 1.25$ m, which allows acquisition of SANS data with low parallax distortions for a maximum of $2\theta_{SANS} = 24°$ [19]. The Q range can be completed to higher Q values with data measured with the WANS detectors.
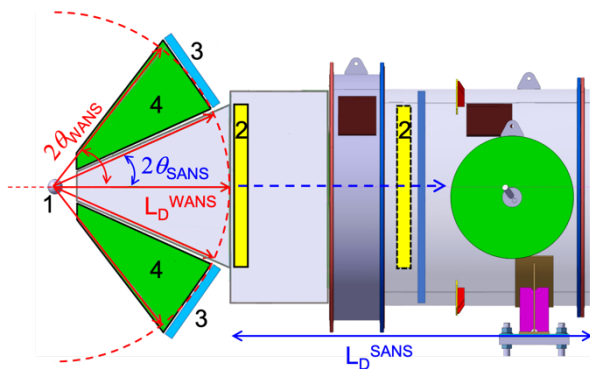
Fig. 7. Schematic representation of the concept of the planned WANS option at KWS-2: the wide-angle detector panels (3) are arranged in a fixed inclined position above and below the beam axis at $L_D^{WANS} = 1.25$ m downstream of the sample (1), so that the scattered neutrons can be detected up to an angle $2\theta_{WANS} = 50°$. The mobile SANS detector (2) that can be moved between $L_D = 1.25$ m and $L_D = 20$ m is marked in yellow. The He boxes (4) in front of the WANS detection arrays are marked in green.

McStas simulations were performed to evaluate the concept of combining SANS and WANS at KWS-2. The crystalline scattering pattern of AgBeh in the high Q region, up to $Q_{max} = 2.0$ Å^{-1}, is characterized by a large number of narrow peaks that make wide-angle scattering test analysis with neutrons difficult, even with a high-resolution approach at a conventional SANS diffractometer. Instead, the fullerene C60 powder in this Q region is characterized by isolated and very sharp crystalline reflections, making such a sample ideal for feasibility tests and simulations of the experimental SANS-WANS approach at KWS-2. We chose to follow the reflection from the crystalline planes (111) that appears in XRD patterns at $2\theta = 10.78°$ [24, 25]. In Q, this crystalline reflection appears isolated at $Q_{C60} = 0.76$ Å^{-1}. In a SANS experiment, this reflection from a fullerene C60 powder sample is observed as a ring at a scattering angle of $2\theta = 19.8°$ when neutrons with a wavelength of $\lambda = 2.8$ Å are used, while in the WANS regime it is observed at $2\theta = 35.7°$ for neutrons with a wavelength of $\lambda = 5.0$ Å.
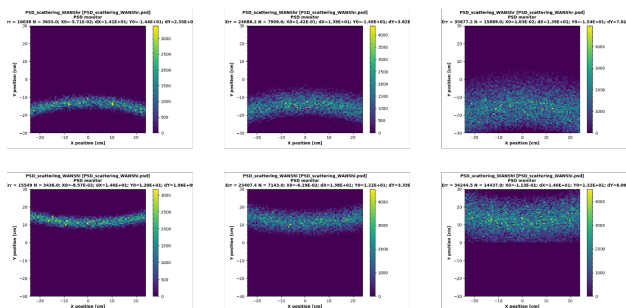

Fig. 8. McStas simulation results of scattering of fullerene C60 samples on two detection panels positioned as indicated in Fig. 7, using neutrons with a wavelength $\lambda = 5$ Å with a resolution of $\Delta\lambda/\lambda = 5\%$ (left panels), 10% (middle panels) and 20% (right panels).

The results of the McStas simulations for the setup schematically shown in Fig. 7 with the detectors at a distance $L_D = 1.25$ m from the sample, in an oblique position with respect to the beam axis, and using the Powder1.comp component of McStas for the fullerene C60 sample are shown in Fig. 8. Different wavelength distributions were used in the simulations, always with $\lambda = 5$ Å. The ring scattering of the powder sample due to the crystalline 111 reflection is well reproduced. As can be seen, the quality of the results obtained at high resolution ($\Delta\lambda/\lambda = 5\%$) suggests that useful structural data on semi-crystalline systems with small crystalline units yielding crystalline reflections above $Q = 1.0$ Å^{-1} can be obtained with this setup using the TOF data acquisition and the resolution chopper of the instrument. Combined with simultaneous SANS data acquisition and the contrast variation technique, this will contribute to a more thorough characterization of such materials. Treatment of the incoherent background was not considered in the McStas simulation because one of the planned ways to work with the WANS detectors at KWS-2 is to use the background chopper and TOF data collection [5] to sort out the neutrons inelastically scattered from the hydrogen-containing samples and thus reduce the incoherent background. Neutrons inelastically scattered from hydrocarbon materials such as polymer or protein solutions contribute significantly to the recorded intensity in a SANS experiment. This contribution is due to incoherent and multiple scattering from hydrogen or deuterium nuclei and contributes as a flat background to the measured data. The proof of principle has been provided elsewhere [5], using the typical high-Q setup at KWS-2, i.e., short input wavelengths, $\lambda = 5$ - 7 Å, and short detection distances, $L_D = 1.1$ - 1.6 m. Positioning the future WANS detectors at KWS-2 at a distance of $L_D = 1.25$ m from the sample will allow the proper TOF conditions to be established for these wavelengths to provide insight into the inelastic scattering and resulting background, which is useful when data collected at high Q do not show a flat profile.

3 Conclusions

The KWS-2 is a classical 40-m pinhole small-angle neutron diffractometer that can cover a wide Q range by varying the sample-to-detector distance between 1 m and 20 m and the wavelength λ between 2.8 and 20 Å. With recent upgrades following the move to the FRMII reactor, the pinhole mode has been combined with the focusing mode using MgF$_2$ lenses, and a wide Q range between 2×10^{-4} and 1.0 Å^{-1} has become available on the instrument, enabling structural studies of complex morphologies with multiple size levels over a broad length scale from nm to micron. Further upgrades to the detection system and sample environment are currently underway. A wide-angle detection option is currently being tested and optimized and will allow measurements over an extended Q-range up to 2.0 Å^{-1}, which will be beneficial for the complete characterization of semi-

crystalline materials and small biological morphologies. The high neutron flux, which is comparable to that at the world-leading SANS instruments, was crucial for optimizing the measurement procedure to make the best use of the beam time. A new versatile system for positioning samples in the beam, consisting of a temperature-controlled carousel with multiple positions, was recently put into operation. It allows samples to be continuously supplied to the instrument and experiments on similar samples or effects to be pooled in a common long experimental session using robotic elements and a storage of sample cuvettes that can be easily renewed by the experimentalist.

References

1. A. Radulescu, V. Pipich, H. Frielinghaus, M-S. Appavou, J. Phys.: Conf. Ser. **351**, 012026 (2012)

2. A. Radulescu, V. Pipich, A. Ioffe, Nucl. Instrum. Methods Phys. Res. Sect. A **689**, 1-6 (2012)

3. A. Radulescu, N. K. Szekely, S. Polachowski, M. Leyendecker, M. Amann, J. Buitenhuis, M. Drochner, R. Engels, R. Hanslik, G. Kemmerling, P. Lindner, A. Papagiannopoulos, V. Pipich, L. Willner, H. Frielinghaus, D. Richter, J. Appl. Cryst. **48**, 1849–1859 (2015)

4. J. E. Houston, G. Brandl, M. Drochner, G. Kemmerling, R. Engels, A. Papagiannopoulos, M. Sarter, A. Stadler, A. Radulescu, J. Appl. Cryst. 51, 323-336 (2018)

5. L. Balacescu, G. Brandl, A. Radulescu, J. Appl. Cryst. **54**, 1217–1224 (2021)

6. Gilles, R., Keiderling, U., Strunz, P., Wiedenmann, A., Fuess, H., Mater. Sci. Forum, **321–324**, 264–269 (2000)

7. Okabe, S., Karino, T., Nagao, M., Watanabe, S., Shibayama, M., Nucl. Instrum. Methods Phys. Res. Sect. A **572**, 853–858 (2007)

8. Grillo, I. (2008). In Soft Matter Characterization, edited by R. Borsali & R. Pecora. Berlin, Heidelberg: Springer.

9. H. Frielinghaus, V. Pipich, A. Radulescu, M. Heiderich, R. Hanslik, K. Dahlhoff, H. Iwase, S. Koizumi, D. Schwahn, J. Appl. Cryst. **42**, 681-690 (2009)

10. B. Krugmann, A. Radulescu, M.-S Appavou, A. Koutsioubas, L. R. Stingaciu, M. Dulle, S. Förster, A. M. Stadler, Scientific Reports, 10, 16691

11. K. Komorowski, A. Salditt, Y. Xu, H. Yavuz, M. Brennich, R. Jahn, T. Salditt, Biophysical Journal **114**, 1908–1920 (2018)

12. B. Hammouda, J. Appl. Cryst. 43, 1474-1478 (2010)

13. G. Brandl, et al., NICOS – The Instrument Control Solution at the MLZ, in Proceedings of the 10th International Workshop on Personal Computers and Particle Accelerator Controls, Karlsruhe, Germany, 14-17 October 2014.

14. S. Koizumi et al., J. Appl. Cryst. 40, s474-s479 (2007)

15. K. Wood et al., J. Appl. Cryst. **51**, 293-314 (2018)

16. S. Takata et al., JPS Conf. Proc. **8**, 036020 (2014)

17. R. K. Heenan et al., Proc. ICANS – XVII, 780-785 (2005).

18. W. T. Heller et al., J. Appl. Cryst. **51**, 242-248 (2018)

19. C. D. Dewhurst et al., J. Appl. Cryst. 49, 1-14 (2016)

20. Sokolova A. et al., J. Appl. Cryst. 52, 1-12 (2019)

21. Schiavone et al., J.Appl. Cryst., in press (2023)

22. https://mlz-garching.de/media/roboter_v1.5.5_short.mp4

23. J. G. Barker and D. F. R. Mildner, J. Appl. Cryst. 48, 1055-1071 (2015)

24. M. Sathish and K. Miyazawa, Cryst. Eng. Comm. **12**, 4146-4151 (2010)

25. A. Sanz, H. C. Wong, A. J. Nedoma, J. F. Douglas, J. T. Cabral, Polymer **68**, 47-56 (2015)